ORIGINAL ARTICLE

Analysis of 3D interaction of a blast wave with a finite wall

A. Gautier[1] · I. Sochet[1] · E. Lapebie[2]

Abstract
The aim of this study is to characterize the interaction of a shock wave with an obstacle. The effect of the length of the obstacle on the shock wave propagation and maximum overpressure is investigated. Several previous studies investigated the use of obstacles such as porous materials, grids, pseudo-perforated walls, triangular wedges, or multi-obstacles as a way to mitigate blast intensity. Here, the focus is on the interaction of an incident shock wave on a single-plate obstacle. This obstacle can be seen as a wall or a low-rise building. The paper presents a small-scale experimental study. The blast wave is created by the detonation of a hemispherical gaseous charge. It is characterized by pressure sensors and a high-speed camera. The pressure sensors record the overpressure and arrival time. The propagation, reflection, and diffraction of the shock wave are analyzed from the pictures produced during the visualization tests.

Keywords Blast wave · Wall · Lateral wave · Bypass wave · Maximum overpressure · Arrival time · Shock wave interaction

1 Introduction

In the literature, the interaction of a shock wave with an obstruction is analyzed according to the different properties of the obstruction. Thus, the isolated obstacle in a highly compressible flow and in the presence of a shock wave can be examined either as an absorbing element or as a perfectly rigid and reflective element. When the obstacle is assumed to be perfectly reflecting, its geometry and dimensions are the parameters chosen to determine its influence on the properties of the transmitted and reflected waves. Maillot et al. [1] experimentally measured the height of the Mach stem appearing downstream of a semi-cylindrical obstacle with a radius of half the hemispherical explosive charge (gas mixture, propane–oxygen). In addition, they noted that overpressure was reduced by about 30% close downstream of the obstacle compared to free-field values, but then increased under the effect of the appearance of the Mach stem (approximately 50 mm downstream of the semi-cylindrical obstacle with a radius of 23 mm) and later recovered its value in

free-field conditions. The Mach stem was considered as the sole cause of the maximum overpressure increase since the infinite length of the semi-cylindrical obstacle makes the diffraction of the shock wave take place in a two-dimensional plane. Therefore, there is no lateral wave that could produce overpressure.

Complex geometries have been analyzed in order to mitigate the incident shock wave. Sha et al. [2] investigated numerically the influence of obstacle geometry on the attenuation of a shock wave. By first studying the effect of the thickness of a rectangular obstacle, they observed that the narrower the obstacle, the faster the attenuation of the incident shock wave. Thus, in order to have the thinnest possible edge while keeping a physically rigid structure, they chose a triangular shape for the obstacle. They then studied the effect of the inclination of the downstream and upstream parts of the triangular obstacle. They found that the inclination of the downstream face had no influence, whereas the upstream face of the triangular obstacle attenuated the shock wave. Thus, by comparing their results with the experimental shock tube tests by Gongora-Orozco et al. [3] for the same obstacle heights and inter-obstacle gap, they showed that triangular obstacles with an obtuse slope on the windward side are more effective than rectangular obstacles in terms of attenuation of the incident shock wave.

In [4], Sochet et al. studied the effect of the inclination of the leading and trailing edges of protective walls on

✉ I. Sochet
   isabelle.sochet@insa-cvl.fr

1 INSA Centre Val de Loire, PRISME, EA4229, 18022
   Bourges Cedex, France

2 CEA, DAM, Gramat, 46500 Gramat, France

the overpressure of blast waves for angles between 20° and 90°. It was found that a 90° angle on the upstream face of the protective barrier had a shielding effect, reducing the maximum downstream overpressure but producing strong reflected overpressures. The 90° angle on the upstream face also avoided the formation of a Mach stem before the incident wave reaches the top of the barrier. A 90° angle on the downstream face of the barrier had the advantage of creating a large expansion wave, which also reduced the maximum overpressure. Blast wall protection was experimentally studied by Rose et al. [5,6], and particular attention was paid to the "shadow" region above the ground downstream of the wall. According to Borgers and al. [7] using numerical means, the "shadow" region represents at least four times the height of the wall.

This paper presents an experimental study of the interaction of a spherical blast wave with an isolated obstacle (called "wall" in the following). Particular attention was paid to the maximum overpressure evolution on the ground downstream of the wall. The only parameter studied was the obstacle length perpendicular to the direction of the shock wave propagation. The chosen walls and the experimental setup are presented in the first part. In the second part, the maximum overpressure is analyzed and is broken down according to its different sources. Then, in the third part a maximum overpressure calculation is suggested to compute the effects downstream of the obstacles.

2 Experimental facilities

2.1 Experimental setup

The experiments were carried out at small scale. The explosion is produced by detonating a gaseous charge (propane–oxygen stoichiometric mixture) in a hemispherical soap bubble. With a radius of 60 mm, the mass m_c of the hemispherical charge is 6.2882×10^{-4} kg. The energy produced by the explosion of this volume of gas is 6.85×10^{-3} MJ. This gaseous explosive charge at small scale is well documented in the literature and can be used as a model. It was used by Rokhy and Soury [8] to validate their numerical method by comparing the experimental results of Sauvan et al. [9] in a confined room with their simulation. The ignition device and the experimental bench are the same as those used in Maillot et al. [1]. This system was optimized to ensure good repeatability. Figure 1 illustrates this repeatability with an example of three overpressure measurements in free field at 203 mm from the center of the explosive charge.

In addition to repeatability, each test had to satisfy a validation criterion. This criterion is a tolerance of 5% on the maximum overpressure measured by a pressure sensor positioned in free field and compared to a reference value.
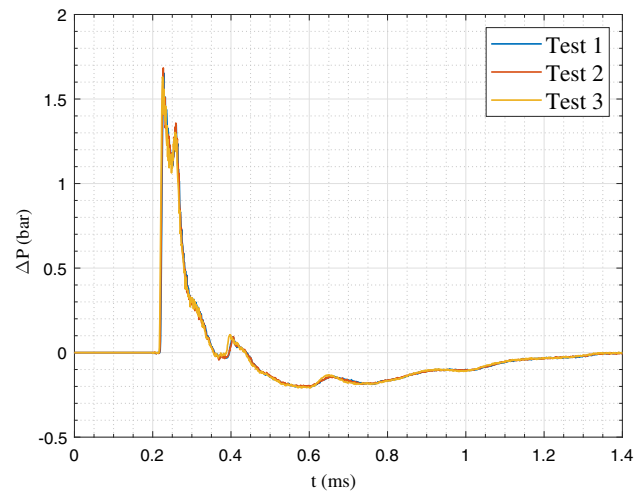

Fig. 1 Overlay of three overpressure measurements in free field

Therefore, all the experimental measurements presented have a constant error margin of 5%.

The flat table, called detonation table, is perforated, in order to install the ignition device and pressure sensors (Fig. 2). Ignition is created by discharging a high voltage to sublimate a tinned copper wire between two electrodes. Sochet et al. [10] provide details on this ignition method.

Visualizations were performed using the shadowgraph method PILS (Pure In Line Shadowscopy) detailed in Hargather et al. [11]. In this method, the light source is coaxial with the optical axis. Light rays are deflected through the shock wave and produce shadows on the retro-reflective screen positioned behind the studied area (Fig. 2). However, the divergence of the light rays forces an optical correction as given by Dewey [12] to measure the free-field propagation of the shock wave. This correction of the shock wave ray depends on the distance between the observed phenomenon and the camera, and on the position of the charge center. In the present study, the parallax error was estimated by the shock wave speed from the pressure sensors and the measurements from the visualization. The parallax error was found to be 1.5%.

2.2 Experimental equipment

The pressure sensors used to measure the properties of the blast wave are piezoelectric PCB 113B26. Acquisition was recorded from 1 ms before the explosion until 5 ms after the explosion with a sampling rate of 1 MHz. In the present study, the pressure sensors are positioned in the axis passing by the center of the charge and the center of the obstacle to simplify the analysis, including one probe isolated in free field (Fig. 2). The distance between each sensor is 100 mm. The first sensor is located between the obstacle and the center of the explosive charge, 103 mm from the latter.
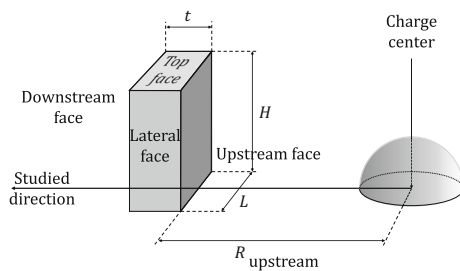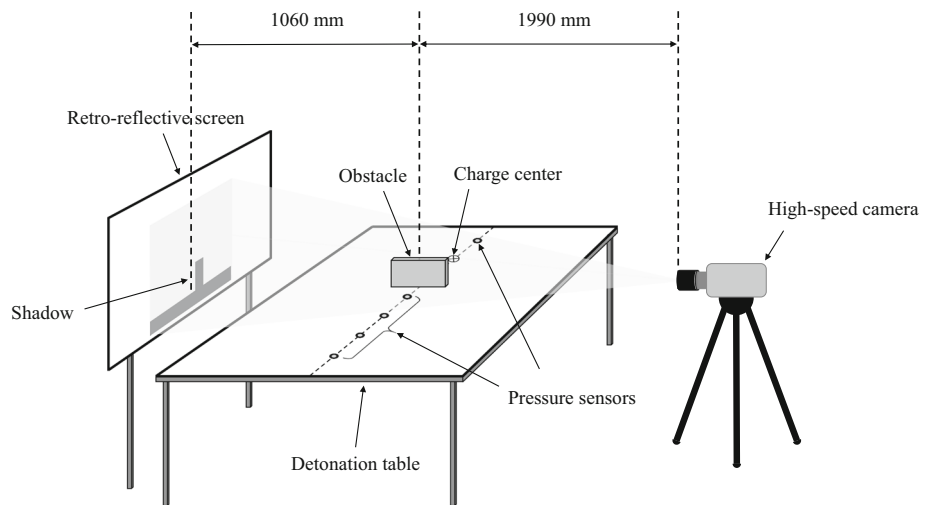
Fig. 2 Experimental bench schema

Fig. 3 Dimension nomenclature of obstacles

Table 1 Classification of obstacles

Obstacle name	t (mm)	L (mm)	H (mm)	L/H
Wall-18-82-82	18	82	82	1.00
Wall-18-100-82	18	100	82	1.22
Wall-18-120-82	18	120	82	1.46
Wall-18-150-82	18	150	82	1.83
Wall-18-168-82	18	168	82	2.05
Wall-18-175-82	18	175	82	2.13
Wall-18-196-82	18	196	82	2.39
Wall-18-250-82	18	250	82	3.05
Wall-18-300-82	18	300	82	3.66
Wall-18-350-82	18	350	82	4.27
Wall-18-400-82	18	400	82	4.88
Wall-18-500-82	18	500	82	6.10

Shock wave visualizations were performed with a high-speed camera Phantom V7.3. In all the experiments, the sample rate was 16,877 pps and the image resolution was 688×456 pixels. With this resolution, an area of 570×217 mm^2 can be visualized. The manufacturer of the fast camera guarantees that there is no distortion, except for images exported in JPEG format due to compression. Hence, once the videos had been recorded, they were exported in AVI format and then processed using the open-source software imageJ.

2.3 Obstacles

In this study, the shock wave interacts with a single obstacle/wall. The nomenclature of the wall dimensions is detailed in Fig. 3 with t for thickness, L for length, H for height, and $R_{upstream}$ the distance between the center of the charge and the upstream face of the wall. In all configurations, $R_{upstream}$, t, and H remain constant at $R_{upstream} = 144$ mm, $t = 18$ mm, and $H = 82$ mm. The length L varies from 82 to 500 mm. The dimensions of the obstacles and their position in relation to the explosive charge make it possible to represent on a small scale an IED (Improvised Explosive Device) explosion facing a fence wall.

The classification of all the walls is presented in Table 1.

3 Analysis of the maximum overpressure

When the incident spherical blast wave, called incident wave (IW), interacts with a finite wall, one part is reflected, and one part diffracts around each face of the obstacle (the two sides and top, see Fig. 3). Around the lateral faces, this part of the blast wave is called lateral wave (LW); the wave diffracting on the top face is called bypass wave (BW). In this study, the maximum overpressure ΔP_{max} is the main blast wave property analyzed. It was measured at different positions in only one direction (studied direction, Figs. 2 and 3). Measurements were then compared to the free field values $\Delta P_{max,FF}$, i.e., when there is no obstruction. One way to compare these measures is to use the relative difference RD. The relative difference of the maximum overpressure is defined as follows:

$$\mathrm{RD} = \frac{\Delta P_{max} - \Delta P_{max,FF}}{\Delta P_{max,FF}} \times 100 \qquad (1)$$

Fig. 4 Relative difference of the maximum overpressure
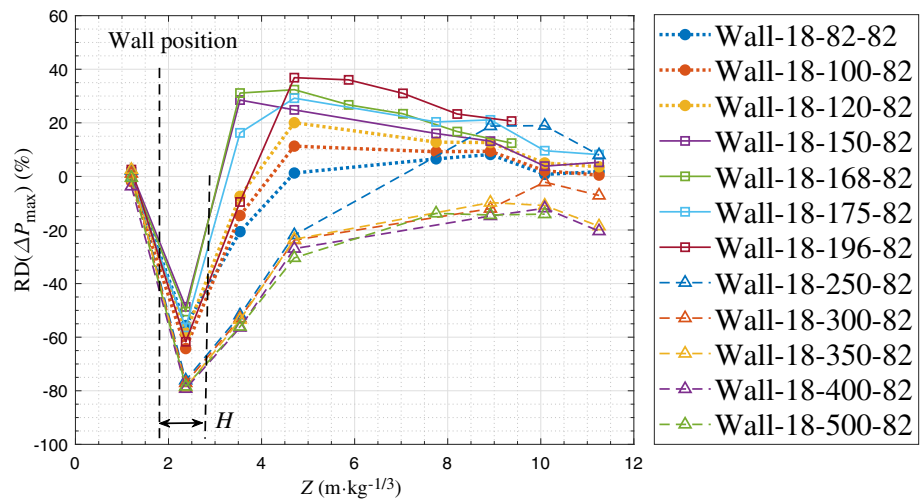
In order to compare experiments at different scales, the reduced distance Z is used throughout this study to express the maximum overpressure and the arrival time evolution, since it has been demonstrated that small-scale experiments are correlated with large-scale experiments (Rigby et al. [13], Dewey and Sochet [14]) using scaled values. In this study, the reduced distance was calculated by dividing R by the cubic root of the charge mass m_c:

$$Z = \frac{R}{\sqrt[3]{m_c}} \qquad (2)$$

The relative difference of the maximum overpressure RD (ΔP_{max}) downstream of the obstacles presented in Table 1 is plotted against the reduced distance Z in Fig. 4.

As shown in Fig. 4, there are different shapes of overpressure evolution downstream of the obstacles. The wall length L governs these differences. Hence, the obstacles were split into three categories:

- $H \leq L < 1.5\,H$, or equivalently $82\,\text{mm} \leq L < 150\,\text{mm}$
- $1.5\,H \leq L < 3\,H$, or $150\,\text{mm} \leq L < 250\,\text{mm}$
- $L > 3\,H$, or $L > 250\,\text{mm}$

In the first category ($H \leq L < 1.5\,H$), increasing the obstacle length increases the maximum overpressure following the initial attenuation. In the second category ($1.5\,H \leq L < 3\,H$), increasing L delays reaching the positive phase of the relative difference RD (ΔP_{max}) downstream of the obstacles. In the third category ($L \geq 3\,H$), the values of the relative difference of the maximum overpressure remain negative. Here, the mitigation effect is greater than in the other categories. Wall-18-250-82 seems to represent the transition criteria from $Z = 7\,\text{m} \cdot \text{kg}^{-1/3}$ because its relative maximum overpressure difference reaches positive values. One can note that the maximum overpressure attenuation is
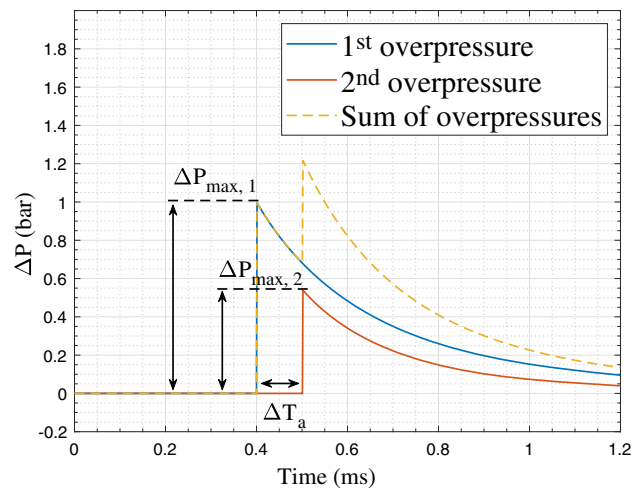

Fig. 5 Schematic illustration of the assumption concerning the sum of overpressures

80% at the nearest pressure sensor downstream of the wall. Contrary to the claims of Borgers et al. [7], the "shadow" region here is estimated to be only once the height of the wall H.

3.1 Retrieval of different overpressure sources

Based on what has been described above, it is interesting to investigate which phenomena are responsible for such a difference between the three obstacle categories. In this section, it is assumed that the overpressures produced by shock waves that consecutively reach a given position add up perfectly. Figure 5 illustrates this assumption. In this illustration, a first shock wave produces a first overpressure. Later, a second shock wave produces a second overpressure. Finally, the resulting overpressure is the sum of the overpressures produced by the two shock waves.
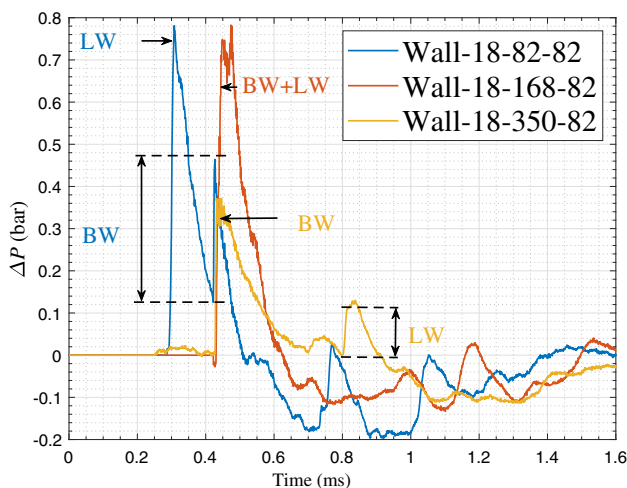
Fig. 6 Overpressure time history at $0.4786 \ \mathrm{m \cdot kg^{-1/3}}$ ($H/2$) downstream of the obstacles

Figure 6 shows the overpressure time history at the distance $H/2$ downstream of three obstacles, i.e., in its shadow area, one from each category. The obstacles are Wall-18-82-82, Wall-18-168-82, and Wall-18-350-82. The relative differences of the maximum value of each overpressure profile are visible in Fig. 4 at $Z = 2.37 \ \mathrm{m \cdot kg^{-1/3}}$.

Figure 6 demonstrates several things which are detailed in Table 2. Finally, one can see that there are three different shock wave schemes:

– The shock wave is a bypass wave BW.
– The shock wave is a couple of lateral waves LWs.

– The shock wave is a combination of the bypass wave BW and the lateral waves LWs.

3.2 Bypass wave BW

The so-called bypass wave is the part of the incident wave that diffracts on the upper side of the obstacle and reflects on the ground. Hence, the bypath path depends on the obstacle height. However, in this study, all the obstacles are the same height: 82 mm. So, the bypass wave BW trajectory is expected to be the same for each obstacle. As the bypass wave does not use the straightway Z, it is expressed against a new reduced distance, the reduced bypass path:

$$
Z_{\mathrm{bypass}} = \sqrt{Z_{\mathrm{upstream}}^2 + \left(\frac{H}{\sqrt[3]{m_{\mathrm{c}}}}\right)^2} \\
+ t + \sqrt{\left(\frac{H}{\sqrt[3]{m_{\mathrm{c}}}}\right)^2 + Z_{\mathrm{downstream}}^2}
$$

(3)

where Z_{upstream} is the reduced scale of the distance R_{upstream} and $Z_{\mathrm{downstream}}$ is the reduced distance downstream of the obstacle.

In order to estimate the bypass wave effects as accurately as possible, arrival time and overpressure are presented only downstream of the obstacles whose length exceeds 250 mm, i.e., obstacles from the third category (see Fig. 7).

As expected, the measured properties are the same downstream of these obstacles. From these measurements, evolution laws can be expressed for a reduced bypass path ranging from $3.2 \ \mathrm{m \cdot kg^{-1/3}}$ to $12.7 \ \mathrm{m \cdot kg^{-1/3}}$. The arrival time and

Table 2 What Fig. 6 demonstrates

| Observations	Demonstration	Conclusion
The shock wave going around Wall-18-82-82 (blue curve) reaches this position quicker than the shock wave going around other obstacles (red and yellow curves)	This means that the distance travelled by the shock wave to go around Wall-18-82-82 is shorter than the distance to go around Wall-18-168-82 and Wall-18-350-82	The first peak overpressure downstream of Wall-18-82-82 is produced by lateral waves LWs
A second shock wave produces overpressure downstream of Wall-18-82-82 at the same arrival time as incident shock waves downstream of other obstacles	This means that the distance travelled by this second shock wave going around Wall-18-82-82 is the same as the distance to go around Wall-18-168-82 and Wall-18-350-82	The second peak overpressure downstream of Wall-18-82-82 and the first
The overpressure produced by the second shock wave downstream of Wall-18-82-82 is the same as the overpressure produced by the incident shock wave downstream of Wall-18-350-82 (yellow curve)	That means that they are the same shock waves and peak overpressure downstream of Wall-18-350-82 are produced by the bypass wave BW	
Even if the length of Wall-18-168-82 is greater than the length of Wall-18-82-82, the maximum value of each overpressure profile (blue and red curves) is the same	This means that there is a combination of several shock waves	Downstream of Wall-18-168-82, lateral waves LWs and the bypass wave BW interact and arrive at the same time
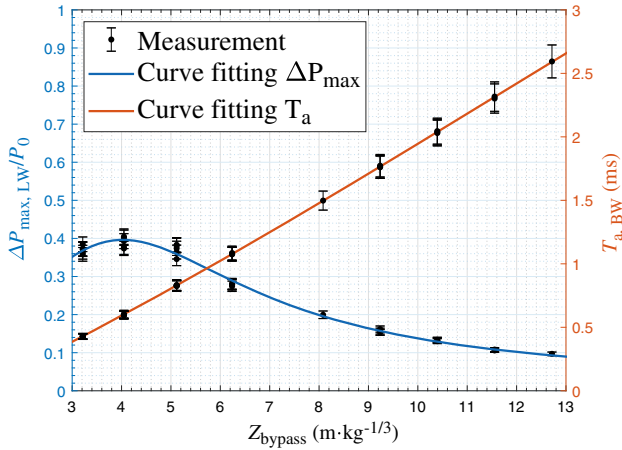
Fig. 7 Measurements of the properties of the bypass wave BW downstream of the obstacles

Fig. 8 Measurements of the properties of the lateral waves LWs downstream of the obstacles

the maximum overpressure of the bypass wave BW are given in (4) and (5), respectively:

$$T_{a,BW} = \frac{0.2477\, Z_{bypass}^2 + 0.3261\, Z_{bypass} - 0.4416}{Z_{bypass} + 4.187} \quad (4)$$

$$\frac{\Delta P_{max,BW}}{P_0} = \frac{0.605\, Z_{bypass} - 1.473}{Z_{bypass}^2 - 6.522\, Z_{bypass} + 19.92} \quad (5)$$

3.3 Lateral waves LWs

The lateral waves are the couple of shock waves that diffract around each lateral face of the obstacle and thus apply a side-on pressure. Unlike the bypass wave, the lateral waves depend on the obstacle length, the only parameter that changes between each obstacle. Hence, the path of the lateral waves varies with the obstacles. Figure 8 shows the properties of the lateral waves against the reduced lateral path $Z_{lateral}$ ranging from 2.6 to 13.9 m · kg$^{-1/3}$. The reduced lateral path is expressed as follows:

$$Z_{lateral} = \sqrt{Z_{upstream}^2 + \left(\frac{L}{2\sqrt[3]{m_c}}\right)^2}$$
$$+ t + \sqrt{\left(\frac{L}{2\sqrt[3]{m_c}}\right)^2 + Z_{downstream}^2} \quad (6)$$

The arrival time evolution is linear and its fitted curve equation is:

$$T_{a,LW} = 0.2223\, Z_{lateral} - 0.3068 \quad (7)$$

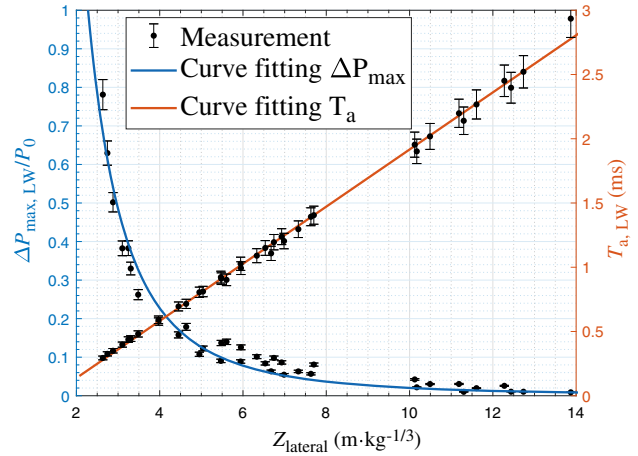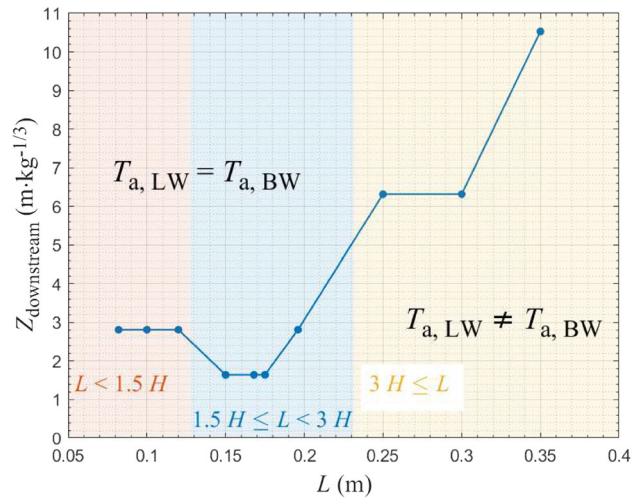The maximum overpressure produced by the lateral waves LWs corresponds to this evolution equation:

Fig. 9 Obstacle lengths and their downstream area where the bypass wave and the lateral waves interact

$$\frac{\Delta P_{max,LW}}{P_0} = 8.774\, Z_{lateral}^{-2.636} \quad (8)$$

3.4 Combination bypass wave/lateral waves

When the bypass wave and the lateral waves arrive at the same time, they interact and create a combination wave. Figure 9 illustrates conditions that make the lateral waves and the bypass wave interact, using data from the pressure sensor analysis. This area is called the interaction area.

Figure 9 is interesting because it shows that the interaction area evolves with the three categories of obstacles. In the first category ($H \leq L < 1.5\,H$), the lateral waves interact together before interacting with the bypass wave. It follows that the interaction area is constant. In the second category ($1.5\,H \leq L < 3\,H$), the lateral waves and the bypass wave interact together almost at the same time. As a result, the
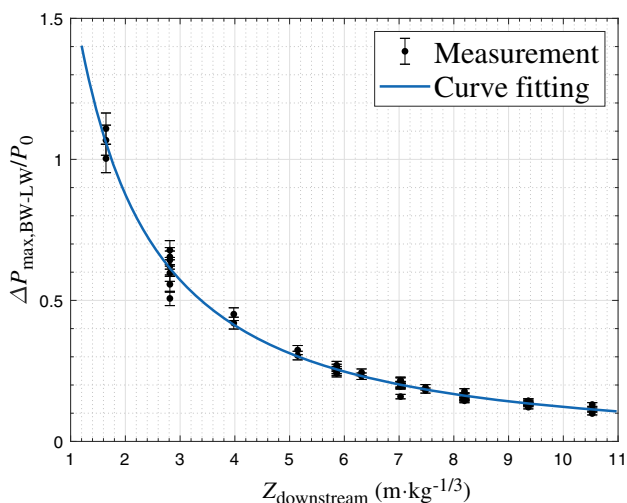
Fig. 10 Maximum overpressure produced by the bypass and lateral waves interaction downstream of the obstacles

interaction area is closer downstream obstacles of the second category than downstream obstacles in the first category. Lastly, in the third category ($L \geq 3\,H$), the lateral waves interact together but they arrive later than the bypass wave. Once they have merged, they will catch up with the bypass wave. Therefore, the greater the length of the obstacle, the farther the interaction zone is from the obstacle.

The maximum overpressure measured in the interaction area is plotted against the reduced distance downstream obstacles in Fig. 10. Here the reduced distance range, where the lateral waves LWs interact with the bypass wave BW downstream of the obstacles, is from 1.7 to $10.5\ \text{m} \cdot \text{kg}^{-1/3}$. The curve fitting the maximum overpressure in Fig. 10 is given by the following equation:

$$
\begin{aligned}
&\frac{\Delta P_{\text{max,BW}-\text{LW}}}{P_0}(Z_{\text{downstream}}) \\
&= \frac{25.6}{Z_{\text{downstream}}^2 + 10.53\, Z_{\text{downstream}} + 4.156}
\end{aligned}
\tag{9}
$$

4 Maximum overpressure calculation

Now that the maximum overpressure produced by the bypass and the lateral waves individually is known, the maximum overpressure downstream of a wall can be estimated by combining these tendency equations. However, Fig. 6 shows that the overpressure of the bypass shock wave and the lateral waves overpressure all add up. Therefore, if the arrival time of the fastest shock wave is close to the arrival time of the slowest wave, the addition of their overpressure increases the maximum overpressure of the signal. Hence, in the maximum overpressure calculation, the difference in arrival time ΔT_a between shock waves must be taken into account.

The maximum overpressure calculation depends on the category of obstacles and is calculated only at the pressure sensors position. Moreover, the purpose of this calculation is to suggest a phenomenological analysis, not to propose an accurate estimate of the maximum overpressure downstream of a wall. The calculation results may therefore contain large errors.

4.1 First category ($H \leq L < 1.5\,H$)

In the first category, the lateral waves LWs go around the wall before the bypass wave BW does. Figure 11 shows the evolution of these waves at four consecutive times after the explosion downstream of the obstacles in the first category (Wall-18-100-82 in this example). In pictures (a), (b), and (c), the bypass wave BW becomes smaller and smaller with time until it disappears in picture (d). As one can see, the bypass wave BW is connected to wave W2. Wave W2 is created by the interaction of the two lateral waves. It means that when lateral waves interact together, they become stronger so that they can be dominant with respect to the bypass wave. Therefore, the bypass wave is absorbed by wave W2. The same thing seems to occur for wave W1 [in fact, there are two W1 waves, as is shown in picture (d)]. This W1 wave is created by the interaction of the bypass wave with each lateral wave. Only one lateral wave should be visible because the bypass by the lateral sides is symmetric. However, both lateral waves are visible because of the parallax. One can note that the wave structure formed by the reflected wave RW, the bypass wave BW, and wave W2 resembles a terminal double-Mach reflection TerDM [15].

Now that interaction between the lateral waves and the bypass wave has been detailed downstream of the obstacles in the first category, a maximum overpressure calculation is proposed. For the first category, the maximum overpressure calculation depends on the distance downstream of the obstacle:

– At $R_{\text{downstream}} < H$

$$
\Delta P_{\text{max}}(Z_{\text{downstream}}) = \Delta P_{\text{max,LW}}(Z_{\text{lateral}})
\tag{10}
$$

– At $R_{\text{downstream}} > H$

$$
\begin{aligned}
\Delta P_{\text{max}}(Z_{\text{downstream}}) = {}& \Delta P_{\text{max,BW}-\text{LW}}(Z_{\text{downstream}}) \\
& - \Delta P_{\text{max,LW}}(Z_{\text{lateral}})
\end{aligned}
\tag{11}
$$

with $\Delta P_{\text{max,LW}}$ and $\Delta P_{\text{max,BW}-\text{LW}}$ calculated from (8) and (9), respectively.

Fig. 11 Organization and evolution of shock waves downstream of the obstacle Wall-18-100-82

(a) Time = 0.474 ms

(b) Time = 0.534 ms

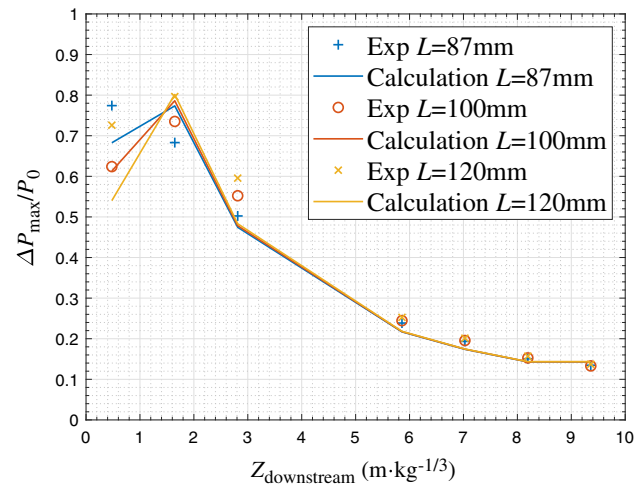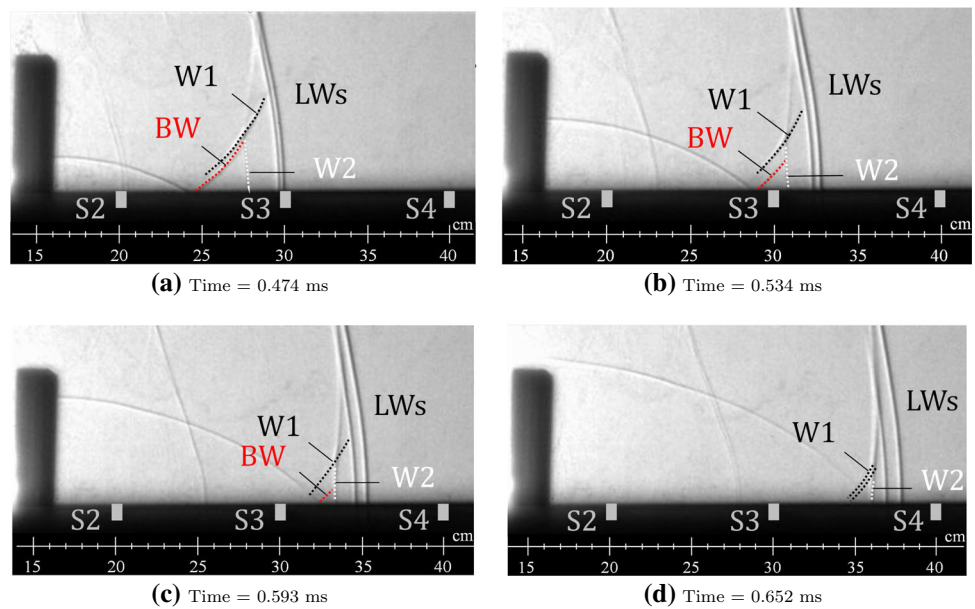**(c)** Time = 0.593 ms

(d) Time = 0.652 ms

Fig. 12 Comparison between experimental and calculated results of the maximum overpressure in category 1

Figure 12 proposes a comparison between the measured maximum overpressure and the calculation from (10) and (11) downstream of the obstacles in the first category. The error produced by the calculation is within the interval $[-25.6\%; 13.2\%]$.

4.2 Second category ($1.5\,H \leq L < 3\,H$)

In the second category of obstacles, the lateral waves LWs go around the obstacle more or less at the same time as the bypass wave does. Therefore, each lateral wave interacts with the other lateral wave as it interacts with the bypass wave. As a result, this new combination produces a maximum over-

pressure higher than downstream of the obstacles in the first category.

– At $R_{downstream} < H$

$$\Delta P_{max}(Z_{downstream}) = 2\,\Delta P_{max,LW}(Z_{lateral}) \quad (12)$$

– At $R_{downstream} > H$

$$\Delta P_{max}(Z_{downstream}) = \Delta P_{max,BW-LW}(Z_{downstream}) \\ - \Delta P_{max,LW}(Z_{lateral}) \quad (13)$$

Figure 13 illustrates the maximum overpressure downstream of the obstacles in the second category from experimental measurement and calculation (12, 13). The error produced by the calculation is within the interval $[-25.3\%; 19.1\%]$.

4.3 Third category ($L \geq 3\,H$)

In the third category, the length of the obstacle is large enough to delay the lateral waves LWs as they do not disturb the bypass wave BW nor its reflection on the ground RW. Hence, the maximum overpressure is produced by the bypass wave (5). Nevertheless, the lateral waves interact together and form a new wave (W2 in Fig. 11). This wave travels faster than the bypass wave, even if its reflection becomes irregular and forms a Mach stem. Therefore, in the third category, as the overpressure produced by the lateral waves is added to the overpressure produced by the bypass wave, the maximum overpressure depends on the delay between the bypass wave
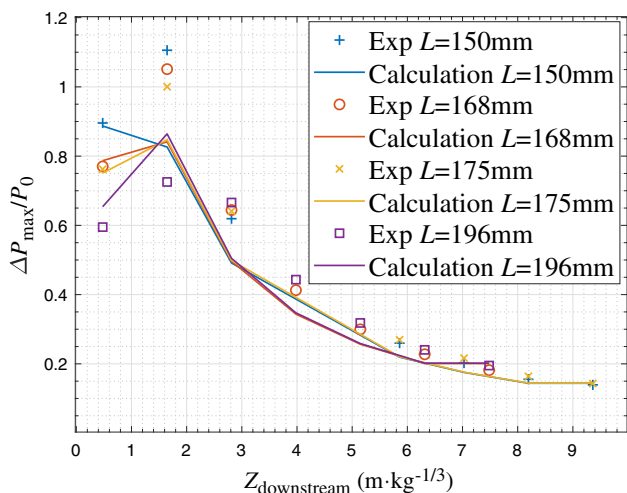
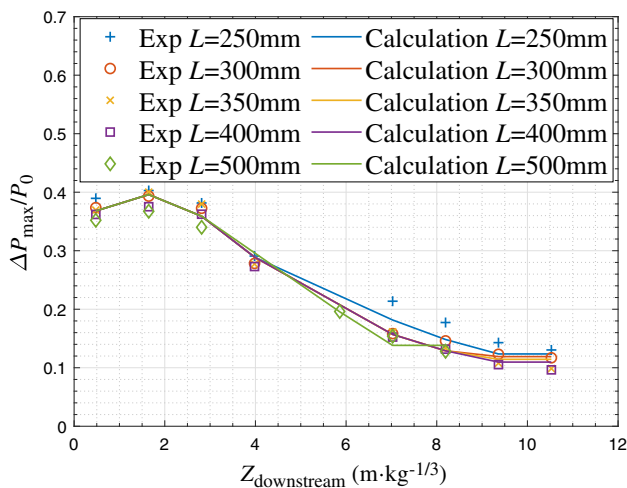**Fig. 13** Comparison between experimental and calculated results of the maximum overpressure in category 2

Fig. 14 Comparison between experimental and calculated results of the maximum overpressure in the category 3

and the lateral waves until they interact all together. Having $\Delta T_a(Z_{\text{downstream}}) = T_{a,\text{BW}}(Z_{\text{bypass}}) - T_{a,\text{LW}}(Z_{\text{lateral}})$,

– While $\Delta T_a > 0.07$ ms

$$\Delta P_{\max}(Z_{\text{downstream}}) = \Delta P_{\max,\text{BW}}(Z_{\text{bypass}}) \tag{14}$$

– Then

$$\Delta P_{\max}(Z_{\text{downstream}}) = \Delta P_{\max,\text{FF}}(Z_{\text{bypass}}) - \Delta P_{\max,\text{BW}}(Z_{\text{bypass}}) \tag{15}$$

with $\Delta P_{\max,\text{FF}}$ the maximum overpressure law without obstruction.

Figure 14 shows the maximum overpressure calculated from (14) and (15) and the measured maximum overpressure

values. The error produced by the calculation is within the interval $[-16.4\%; 16.1\%]$. Here, the estimate of the maximum overpressure is better than for the calculation of the first two categories. This can be explained by the fact that the lateral waves do not act on the maximum overpressure.

5 Conclusion

In this study, the interaction of an isolated finite-dimensional wall with a spherical blast wave has been investigated in order to understand the effects of its lateral dimension (length). Using different obstacles of the same height (82 mm) and for a range of lengths from 82 to 500 mm, the influence of the obstacle length on the maximum overpressure was determined. It was observed that the protective effect occurs in the area close downstream of the obstacle. The maximum protection zone extends over a distance close to the height of the walls H projected to the ground downstream of them. However, depending on the length of the walls, the protective effect does not last. Indeed, downstream of an obstacle whose length $L < 3\,H$, the maximum overpressure becomes much stronger (up to 40%) than in free field. Therefore, it is assumed that this mitigation is canceled by lateral waves when they have caught up with the bypass wave. One can hypothesize that the maximum overpressure is mitigated downstream of an "infinite" obstacle because there is no lateral wave.

Thanks to the distinction between the overpressure produced by the bypass wave and the overpressures produced by the lateral waves in the overpressure measured by each pressure sensor, a calculation of the maximum overpressure is proposed depending on the obstacle length. The difference between measurement and calculation is reasonable $(-25\%$ to $+20\%$ error). Finally, this paper proposes an analysis of phenomena observed downstream of a wall, considering the effect of the bypass wave and the lateral waves on the maximum overpressure.

References

1. Maillot, Y., Sochet, I., Vinçont, J-Y., Grillon, Y.: Experimental evaluation of a shock wave propagation impacting surface irregularity. 25th International Symposium on Military Aspects of Blast and Shock (MABS), The Hague, The Netherlands, 23–28 September (2018)
2. Sha, S., Chen, Z., Jiang, X.: Influences of obstacle geometries on shock wave attenuation. Shock Waves **24**, 573–582 (2014). https://doi.org/10.1007/s00193-014-0520-9
3. Gongora-Orozco, N., Zare-Behtash, H., Kontis, K.: Experimental studies on shock wave propagating through junction with grooves.

47th AIAA Aerospace Sciences Meeting including The New Horizons Forum and Aerospace Exposition, Orlando, FL, AIAA Paper 2009-327 (2009). https://doi.org/10.2514/6.2009-327

4. Sochet, I., Eveillard, S., Vinçont, J.Y., Piserchia, P.F., Rocourt, X.: Influence of the geometry of protective barriers on the propagation of shock waves. Shock Waves **27**, 209–219 (2017). https://doi.org/10.1007/s00193-016-0625-4

5. Rose, T.A., Smith, P.D., Mays, G.C.: The effectiveness of walls designed for the protection of structures against airblast from high explosives. Proc. Inst. Civ. Eng. -Struct. Build. **110**, 78–85 (1995). https://doi.org/10.1680/istbu.1995.27306

6. Rose, T.A., Smith, P., Mays, G.C.: Design charts relating to protection of structures against airblast from high explosives. Proc. Inst. Civ. Eng. -Struct. Build. **122**, 186–192 (1997). https://doi.org/10.1680/istbu.1997.29307

7. Borgers, J., Vantomme, J., van der Stoel, A.: Blast walls reviewed. 21th International Symposium on Military Aspects of Blast and Shock (MABS), Jerusalem, Israel, 3–8 October (2010)

8. Rokhy, H., Soury, H.: Investigation of the confinement effects on the blast wave propagated from gas mixture detonation utilizing the CESE method with finite rate chemistry model. Combust. Sci. Technol. 1–18 (2021). https://doi.org/10.1080/00102202.2021.1905632

9. Sauvan, P.E., Sochet, I., Trélat, S.: Analysis of reflected blast wave pressure profiles in a confined room. Shock Waves **22**, 253–264 (2012). https://doi.org/10.1007/s00193-012-0363-1

10. Rocourt, X., Sochet, I.: Exploding wires. In: Sochet, I. (ed.) Blast Effects: Physical Properties of Shock Waves, pp. 73–87. Springer, Cham (2018)

11. Hargather, M.J., Settles, G.S.: Retroreflective shadowgraph technique for large-scale flow visualization. Appl. Opt. **48**, 4449–4457 (2009). https://doi.org/10.1364/AO.48.004449

12. Dewey, J.M.: Explosive flows: shock tubes and blast waves. Handbook of Flow Visualization (1st ed.), pp. 481–497. Hemisphere Publishing Corp. (1989)

13. Rigby, S.E., Tyas, A., Fay, S., Clarke, S.D., Warren, J.A.: Validation of semi-empirical blast pressure predictions for far field explosions—is there inherent variability in blast wave parameters? 6th International Conference on Protection of Structures Against Hazards, Tianjin, China, 16–17 October (2014)

14. Dewey, J.M., Sochet, I.: Analysis of the blast waves from the explosions of stoichiometric, rich, and lean propane/oxygen mixtures. Shock Waves **31**, 165–173 (2021). https://doi.org/10.1007/s00193-021-01005-x

15. Ben-Dor, G.: Shock Wave Reflection Phenomena. Springer, Berlin (2007)